

# Reservoir Computing on Spin-Torque Oscillator Array

Taro Kanao,\* Hirofumi Suto, Koichi Mizushima, Hayato Goto, Tetsufumi Tanamoto, and Tazumi Nagasawa  
Corporate Research and Development Center, Toshiba Corporation, Kawasaki 212-8582, Japan

(Dated: December 22, 2023)

We numerically study reservoir computing on a spin-torque oscillator (STO) array, describing magnetization dynamics of the STO array by a nonlinear oscillator model. The STOs exhibit synchronized oscillation due to coupling by magnetic dipolar fields. We show that the reservoir computing can be performed by using the synchronized oscillation state. Its performance can be improved by increasing the number of the STOs. The performance becomes the highest at the boundary between the synchronized and disordered states. Using the STO array, we can achieve higher performance than an echo-state network with similar number of units. This result indicates that the STO array is promising for hardware implementation of reservoir computing.

## I. INTRODUCTION

Reservoir computing [1–3], a framework of machine learning, has attracted much attention for realizing a high-performance real-time computing. The reservoir computing utilizes complex dynamics of interacting nonlinear units. In the reservoir computing, only output weights are learned in an external computer. This feature allows hardware implementations of the reservoir computing, as well as reduction of computational costs in learning process. The hardware implementations have been proposed in several physical systems, such as analog electronic circuits [4], optical systems [5, 6], quantum-bit systems [7], and magnetic systems [8–10]. Although these systems have shown good potentials for the reservoir computing, further improvements of computational capacities, operation speed, hardware size, energy consumption, and their balance have been required for practical applications.

Recently, the reservoir computing on spin-torque oscillators (STOs) [11, 12] has been reported [13–15]. (Applications of the STOs to other types of computing have also been proposed [16–22].) An STO is a nonlinear auto-oscillator with a power-dependent frequency shift. The STO exhibits microwave oscillation induced by a spin-polarized direct current via a spin-transfer torque, yielding microwave magnetic and electromagnetic fields. Compared with the above other systems, the STOs have advantages of nanosecond-scale fast dynamics, nanometer-scale size, and low energy consumption. The microwave fields lead the STOs to interact with each other in an array. Although the use of many interacting STOs is expected to achieve higher performance due to complex dynamics of many degrees of freedom, a *single* STO has been assumed in the previous studies of the STO reservoir computing [13–15].

In this paper, we investigate the reservoir computing on the array of the STOs coupled by magnetic dipolar fields, as shown in Fig. 1, where the couplings naturally appear when the STOs are integrated closely with each

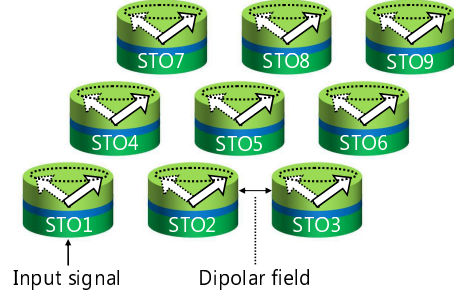


FIG. 1. Schematic of a spin-torque oscillator (STO) array.

other. We perform numerical experiments of the reservoir computing utilizing a nonlinear oscillator model [12] corresponding to the STO array. As a result, we show that the reservoir computing can be performed in the synchronized oscillation state and its performance can be improved with the number of the STOs. The highest performance is obtained at the boundary between the synchronized and disordered states. The performance can become higher than a standard neural network model known as an echo-state network (ESN) [1, 2].

## II. RESERVOIR COMPUTING ON STO ARRAY

### A. Model of STO array

We align the STOs on a square lattice as shown in Fig. 1. In this work, we assume that the STOs exhibit out-of-plane precession [23]. These STOs emit large microwave dipolar fields [24] and output signals due to the magnetoresistive effect [25, 26], which respectively lead to strong couplings between the STOs and a high signal-to-noise ratio at measurements. The oscillations of the STOs synchronize with the same phase [27–29]. [We show in Appendix A an example of such synchronized oscillations by a numerical simulation based on the Landau-Lifshitz-Gilbert-Slonczewski (LLGS) equation [30].]

For the reservoir computing, we utilize dynamics of oscillation powers and phases (or frequencies) of the STOs [13–15]. To calculate these dynamics, we use the

\* taro.kanao@toshiba.co.jp

corresponding nonlinear oscillator model [12, 31], which can capture the essential features of the dynamics of the STOs including the synchronization [32], irrespective of detailed magnetization configuration of the STOs. The nonlinear oscillator model can be derived from the LLGS equation on certain assumptions. (See Appendix B for details.) The powers and frequencies of the STOs usually vary slowly compared with the oscillation itself [12, 24], and fast oscillation components can be eliminated in the nonlinear oscillator model. Thus this model allows us to reduce computational costs for the simulation.

The nonlinear oscillator model for  $N$  STOs is written as [12]

$$\frac{dc_i}{dt} = -i\delta\omega_i(p_i)c_i - \Gamma_i(p_i)c_i - i \sum_{j=1, j \neq i}^N \Omega_{ij}c_j, \quad (1)$$

where  $t, c_i, \delta\omega_i(p_i), \Gamma_i(p_i)$ , and  $\Omega_{ij}$  ( $i = 1, 2, \dots, N$ ) are time, complex amplitudes representing slowly-varying magnetization dynamics, nonlinear frequency shifts originating from magnetic anisotropy, effective damping rates taking account of Gilbert damping and the spin-transfer torque, and coupling strengths between the STOs yielded by the dipolar fields, respectively. Here, a uniform high-frequency oscillation factor has been eliminated (see Appendix B).  $\delta\omega_i(p_i)$  and  $\Gamma_i(p_i)$  are supposed to depend on a dimensionless oscillation power  $p_i = |c_i|^2$ . Assuming linear dependence of  $\delta\omega_i(p_i)$  and  $\Gamma_i(p_i)$  on  $p_i$  [12, 31], we express

$$\delta\omega_i(p_i) = N_f(p_i - p_{i0}), \quad (2)$$

$$\Gamma_i(p_i) = \frac{\Gamma_p}{p_{i0}}(p_i - p_{i0}) - \xi_i(t), \quad (3)$$

where  $p_{i0}, N_f, \Gamma_p$ , and  $\xi_i(t)$  are a stationary oscillation power, a nonlinear frequency shift, a damping rate of power [12], and a modulation by an input signal, respectively, in a unit of frequency.  $\delta\omega_i(p_i)$  and  $\Gamma_i(p_i)$  describe properties of the single STO, and  $\delta\omega_i(p_{i0}) = \Gamma_i(p_{i0}) = 0$  at its stationary state for a constant current. We apply the input signal to the current, which leads to modulation of  $\Gamma_i(p_i)$  via the spin-transfer torque. Equations (2) and (3) can be regarded as linear approximations of  $\delta\omega_i(p_i)$  and  $\Gamma_i(p_i)$  for small deviations of  $p_i$  from  $p_{i0}$ .

In the array, the dipolar fields between the nearest-neighbor STOs  $\Omega$  and next-nearest-neighbor  $\Omega/\sqrt{8}$  are taken into account, as the dipolar field is inversely proportional to the cube of distance. Differences in the STOs are modeled by  $p_{i0}$  of a gaussian random variable with mean of  $p_0$ . In this work, the input signal is applied on an STO at the corner of the array, STO1 shown in Fig. 1, and thus only  $\xi_1(t)$  is modulated and  $\xi_i(t) = 0$  for  $i \neq 1$ . Based on reported values [31, 33], we choose the following values:  $p_0 = 0.5$ ,  $N_f/(2\pi) = 0.1$  GHz,  $\Gamma_p = 0.1$  ns<sup>-1</sup>,  $|\xi_1(t)| < 0.1$  ns<sup>-1</sup>, and  $\Omega = -0.1$  ns<sup>-1</sup>, unless otherwise stated. The value of  $\Omega$  is estimated in Appendix B. The standard deviation of  $p_{i0}$  is set to 0.01. The denominator  $p_{i0}$  in Eq. (3) is approximated by  $p_0$ . Equation (1) is numerically integrated with an initial condition  $c_i = \sqrt{p_0}$ ,

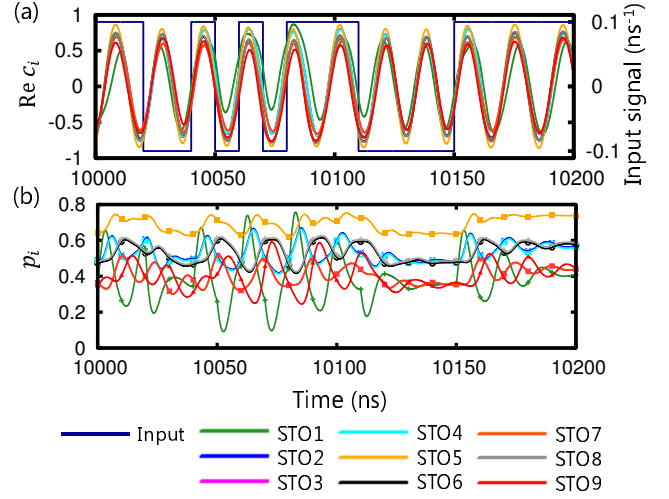


FIG. 2. (a) Waveforms of input signal and real parts of  $c_i$  of 9 STOs for sampling time  $T_s = 10$  ns. (b) Oscillation powers  $p_i$  in the same condition. Measured values of  $p_i$  are indicated by symbols.

which is equivalent to all the magnetizations of STO free layers in the same direction. This situation can be realized in a strong uniform external field.

The reservoir computing utilizes dynamics in waveforms induced by the input signals. Figure 2 shows examples of waveforms of 9 STOs obtained by Eq. (1). The waveforms after a sufficiently long time are shown. The oscillation of  $\text{Re } c_i$  in Fig. 2(a) is induced by the terms of  $\delta\omega_i(p_i)$  and  $\Omega_{ij}$  in Eq. (1). It can be seen that oscillation phases nearly synchronize. Fluctuations of the oscillations are induced by the input signal. Since the input signal is applied on STO1, the power of STO1 is directly modulated by the input signal as in Fig. 2(b). The effects of the input signal propagates to the other STOs. When the input signal is a constant, the dynamics of the powers damp in several tens of nanoseconds. The time scale of the damping of the powers is determined by  $1/\Gamma_p (= 10$  ns). The waveforms of the STOs at symmetric positions (see Fig. 1), (STO2 and 4), (STO3 and 7), and (STO6 and 8), almost overlap, but not completely, because of the deviation of  $p_{i0}$ .

## B. Reservoir computing

Next, we explain the reservoir computing on the STO array. We evaluate its performance by following the setting used in Ref. [7]. The  $k$ th input signal  $s_k$  is introduced into the STO1 with a rate  $1/T_s$  during the time interval between  $T_s(k-1)$  and  $T_sk$ . The powers are measured at the last edge of each interval, in order to fully incorporate effects of the latest signal. The measured values are denoted by  $x_{ki} = p_i(T_sk)$ . Output data are  $y_k = \sum_{i=0}^N x_{ki}w_i$ , where  $w_i$  is the  $i$ th weight for the reservoir computing, and  $x_{k0} = 1$  is introduced for treating a

constant term. The weights are determined in a training process by minimizing  $\sum_k (y_k - \bar{y}_k)^2$ , so that a target series  $\bar{y}_k$  is reproduced. Such  $w_i$  are given by  $\mathbf{w} = X^+ \bar{\mathbf{y}}$ , where  $X$ ,  $\mathbf{w}$ , and  $\bar{\mathbf{y}}$  are a matrix or column vectors with components  $x_{ki}$ ,  $w_i$ , and  $\bar{y}_k$ , respectively, and  $X^+$  is the Moore-Penrose pseudo-inverse matrix of  $X$  [7]. The dynamics of the STO array is calculated for the time of  $5000T_s$ . The first  $1000T_s$  is discarded, and the subsequent  $3000T_s$  and the last  $1000T_s$  are used for the training and the evaluation, respectively.

We evaluate the performance by using short-term memory (STM) and parity-check (PC) tasks [7, 10, 14]. [We also evaluate a nonlinear autoregressive moving average (NARMA) task [7, 34] and show the result in Appendix C.] For the STM and PC tasks,  $s_k$  is a random sequence of 0 and 1. We convert  $s_k$  to  $\xi_1(t)$  by a square wave with value  $\xi_1(t) = 0.1(2s_k - 1) \text{ ns}^{-1}$ . By the STM and PC tasks, capacities of memory and nonlinearity, which are necessary for more general tasks, are evaluated. The targets of these tasks are respectively  $\bar{y}_k = s_{k-\tau}$  and  $\bar{y}_k = Q(\sum_{l=0}^{\tau} s_{k-l})$ , for  $\tau = 0, 1, 2, \dots$ . Parity function  $Q(S)$  is 0 for even  $S$  and 1 for odd. The capacities are measured by  $C = \sum_{\tau=0}^{\tau_{\max}-1} C_{\tau}$ , where  $C_{\tau}$  is the square of the correlation coefficient of  $\bar{y}_k$  and  $y_k$  called a  $\tau$ -delay capacity ( $0 \leq C_{\tau} \leq 1$ ). Here,  $\tau_{\max} = 500$ . A larger  $C_{\tau}$  means higher performance, and  $C_{\tau}$  becomes maximum value 1 when  $\bar{y}_k = y_k$ . The performances are evaluated for 20 sets of  $(p_{i0}, s_k)$ , and the average values of the performances and standard deviations are calculated.

### III. RESULTS AND DISCUSSION

#### A. Performance improvement with increasing $N$

Figures 3(a) and 3(b) show the STM and PC capacities as a function of the number of the STOs  $N$  and the sampling time  $T_s$ . The STM capacity increases with  $N$  in the range shown ( $N \leq 400$ ). The PC capacity saturates at large  $N$ . Behaviors of the capacities at larger  $N$  are discussed below. The capacities depend on  $T_s$ . The STM capacity is larger for shorter  $T_s$ , because time necessary for computing is shorter and the computing is finished before effect of input signals decays. On the other hand, the PC capacity is larger for longer  $T_s$ , because the longer  $T_s$  allows larger variations of the powers such that nonlinear effects appear. The STM and PC capacities saturate for  $T_s \lesssim 1 \text{ ns}$  and  $T_s \gtrsim 100 \text{ ns}$ , respectively.

The data in Figs. 3(a) and 3(b) are summarized in Fig. 3(c). The capacities are distributed below the curve on which the product of the STM and PC capacities is a constant (of 85), implying a trade-off relation between the STM and PC capacities. This kind of relation has been reported as the memory-nonlinearity trade-off [35].

The largest values of the STM and PC capacities obtained here are 46.4 at  $N = 400$  and  $T_s = 2 \text{ ns}$ , and 6.4 at  $N = 196$  and  $T_s = 50 \text{ ns}$ , respectively. These values are larger than the values by the ESN with 500 units

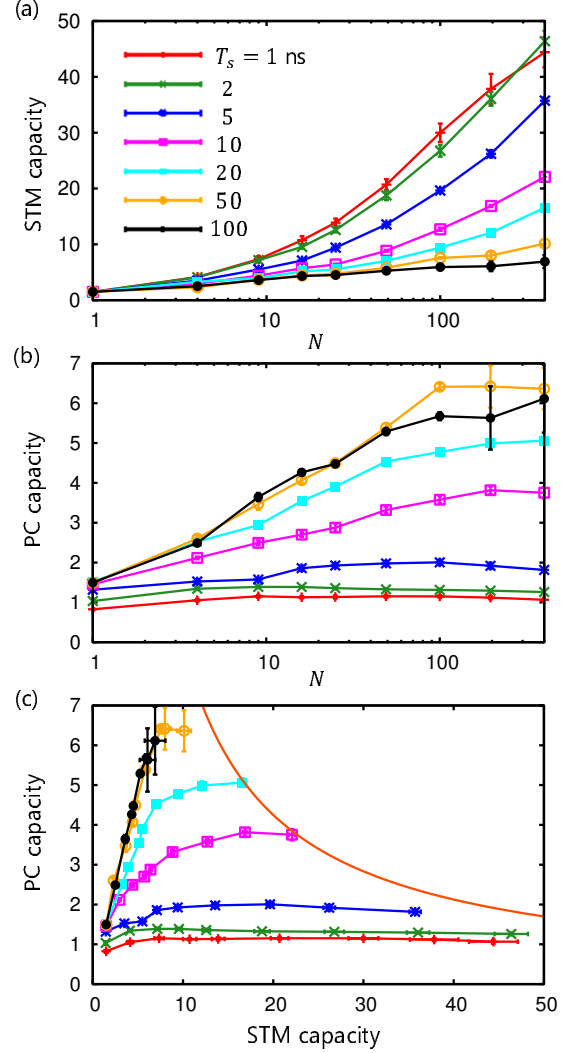


FIG. 3. (a) Short-term memory (STM) and (b) parity-check (PC) capacities as a function of number of STOs  $N$  and sampling time  $T_s$ .  $T_s$  are indicated by common symbols (colors) for (a)-(c). (c) STM capacity in (a) vs PC capacity in (b).

reported in Ref. [7], which are about 17.6 and 6.0, respectively. Remarkably, the largest value of the STM capacity here is larger than twice the value of the ESN.

Figure 4 shows the capacities at each  $\tau$  (the  $\tau$ -delay capacities) for  $N = 400$ . The capacities decrease from 1 to 0 with increasing  $\tau$  for  $T_s \geq 10 \text{ ns} = 1/\Gamma_p$ . The capacities for  $T_s < 1/\Gamma_p$  are small compared with 1 even at small  $\tau$ , owing to transient dynamics induced by the input signals. The STM capacities for  $T_s \leq 2 \text{ ns}$  show finite values at large  $\tau$ , indicating that the effects of the input signals remain.

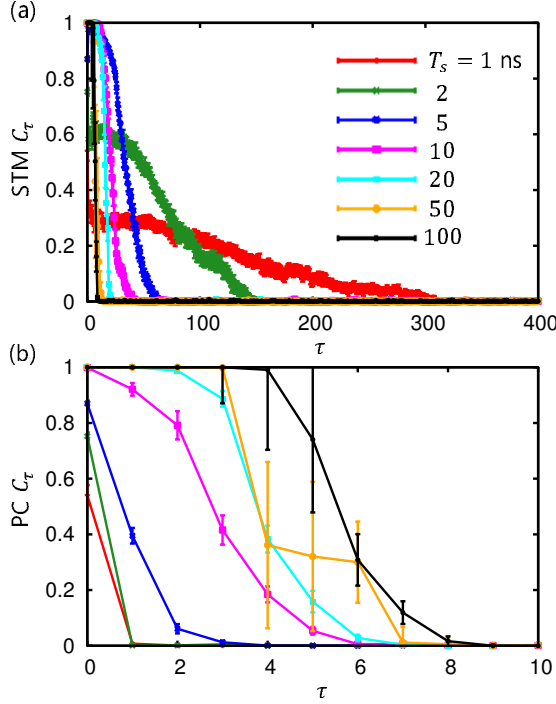


FIG. 4. (a) STM and (b) PC capacities  $C_\tau$  as a function of  $\tau$  for  $N = 400$ .

### B. Performance enhancement near transition

Finally, we investigate the coupling dependence of the STM and PC capacities, and find that the capacities strongly depend on the coupling strength. Figures 5(a) and 5(b) show the STM and PC capacities as a function of the coupling strength  $|\Omega|$  and  $N$  for  $T_s = 5$  ns. The largest capacities appear around  $|\Omega| = 0.14$  ns $^{-1}$ .

To clarify the reason for these dependences of the capacities, we examine oscillation states of the STO array under the corresponding conditions. The oscillation states are characterized by an order parameter  $\rho$  [36, 37] and an average power  $\bar{p}$ ,

$$\rho = \frac{1}{N} \left| \sum_{i=1}^N \frac{c_i}{|c_i|} \right|, \quad (4)$$

$$\bar{p} = \frac{1}{N} \sum_{i=1}^N |c_i|^2, \quad (5)$$

which are shown in Figs. 5(c) and 5(d), respectively. The order parameter  $\rho$  characterizes uniformity of the oscillation phase, and becomes the largest value 1 when all the STOs are perfectly synchronized.

Figure 5(c) shows that  $\rho$  is nearly 1 in most region, indicating that all  $c_i$  have nearly the same phases and thus the oscillations are synchronized.  $\rho$  decreases as  $N$  increased for the same  $|\Omega|$ . The region where the STM and PC capacities are finite in Figs. 5(a) and 5(b) are included in the region where  $\rho$  is rather large ( $\rho \gtrsim 0.5$ )

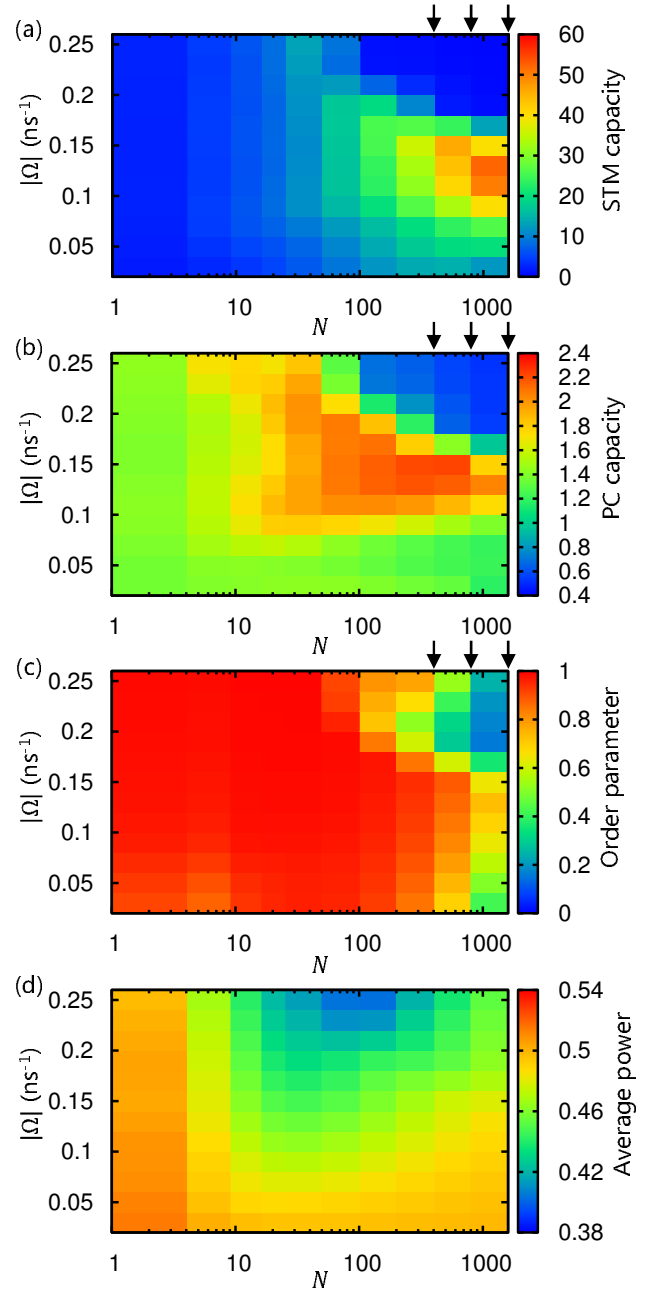


FIG. 5. (a) STM and (b) PC capacities, and (c) order parameter  $\rho$  and (d) average power  $\bar{p}$  as a function of  $N$  and coupling strength  $|\Omega|$  for  $T_s = 5$  ns. Arrows indicate  $N$  of which data are plotted in Fig. 6. The order parameter and the average power are averaged in the same way as the STM and PC tasks.

in Fig. 5(c).

To see more clearly the relation between the performance and the oscillation state, we plot the capacities and the order parameter as a function of  $|\Omega|$  in Fig. 6, where  $N = 400, 784$ , and  $1600$ . As shown in Figs. 6(a) and 6(b), with increasing  $|\Omega|$  the STM and PC capacities almost monotonically increase for  $|\Omega| \lesssim 0.15$  ns $^{-1}$

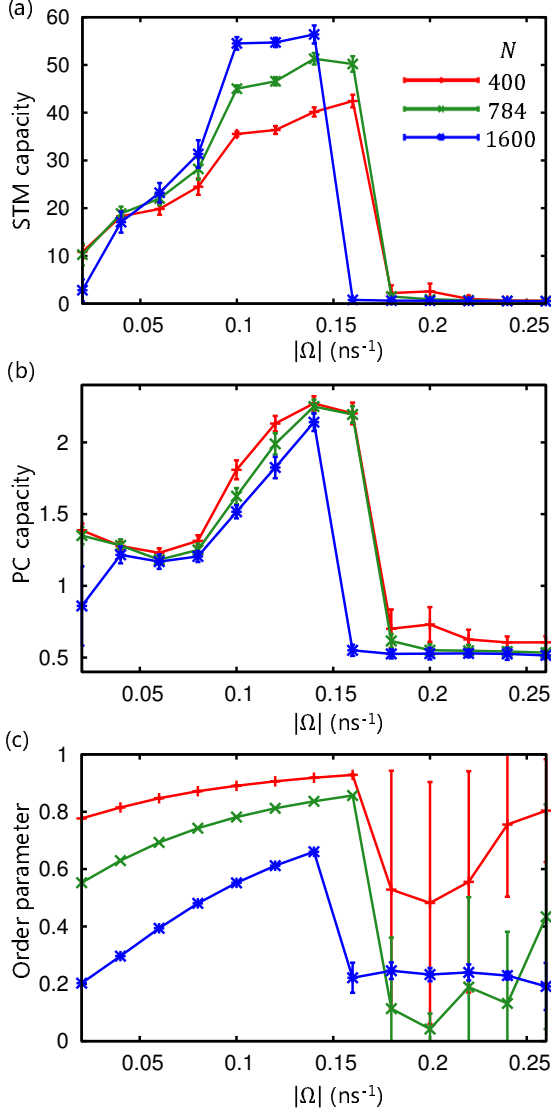


FIG. 6. (a) STM and (b) PC capacities, and (c) order parameter  $\rho$  as a function of  $|\Omega|$  for  $T_s = 5$  ns. Error bars indicate standard deviations for 20 sets of  $(p_{i0}, s_k)$ .

and then suddenly decrease. As shown in Fig. 6(c), the order parameter  $\rho$  also exhibits similar behavior, which indicates a transition from the synchronized oscillation state to a disordered state around  $|\Omega| = 0.15$  ns $^{-1}$  (see below for details). From the results of Figs. 5 and 6, we conclude that the reservoir computing can be performed in the synchronized oscillation state of the STO array and the performance is the highest near the transition to the disordered state, which is consistent with the reported behavior that the capacities of reservoir computing can be enhanced at the edge of this kind of transition [3, 4].

The dependence of the oscillation state on the coupling strength observed in Fig. 6(c) can be understood as follows. The explanation is divided for small and large  $|\Omega|$ . For small  $|\Omega|$ , the power is almost constant  $\bar{p} \simeq p_0 = 0.5$

as seen in Fig. 5(d), and thus the phase freedom is important. Then, the model of Eq. (1) can be reduced to a 2-dimensional Kuramoto model with a short-range interaction [12, 36, 37]. On this Kuramoto model, it has been known that stronger couplings lead to more ordered synchronization while a larger number of oscillators cause more disordered oscillation state [29, 38]. These results on the Kuramoto model can explain the dependence of  $\rho$  on  $|\Omega|$  and  $N$  for  $|\Omega| \lesssim 0.15$  ns $^{-1}$  in Fig. 6(c), where  $\rho$  increases with  $|\Omega|$  and decreases with  $N$ . For large  $|\Omega|$ , on the other hand, the average power deviates from  $p_0 = 0.5$  as seen in Fig. 5(d), and thus nonlinear effects of  $\delta\omega_i(p_i)$  and  $\Gamma_i(p_i)$  in Eq. (1) can appear. In this situation, it has been known that the power degree of freedom causes disordered unsteady states including chaotic states [37, 39]. In these states the synchronization is suppressed, which corresponds to low  $\rho$  for  $|\Omega| \gtrsim 0.15$  ns $^{-1}$  in Fig. 6(c). The disordered unsteady states [37, 39] can also explain the large standard deviations observed for the same region in Fig. 6(c), which indicates that the oscillation states are sensitive to the small changes in the conditions. Between the synchronized state and the disordered state for small and large  $|\Omega|$  respectively, the transition occurs, causing sharp change in  $\rho$ .

The decrease of  $\rho$  with increasing  $N$  is due to the short-range interaction between the STOs. By designing the STOs in the array to couple through long-range interaction, e.g. by using a common electrode [20],  $\rho$  can be finite for large  $N$  [36, 37], allowing the synchronization of large number of STOs.

#### IV. SUMMARY AND OUTLOOK

We have investigated the reservoir computing on the STO array coupled by the dipolar fields. The numerical experiments of the reservoir computing are performed by using the corresponding nonlinear oscillator model, which exhibits the synchronized oscillation. As a result, we have shown that the performance of the reservoir computing is improved by increasing the number of the STOs in the synchronized oscillation state. The values of the STM and PC capacities for  $N \leq 400$  can be larger than those of the ESN for 500 units. In particular, the maximum STM capacity is larger than twice that of ESN. The largest capacities are obtained at the boundary between the synchronized and disordered states. We believe that the results will be explained by the enhancement of the capacities at the edge of chaos. The present results indicate that the STO array is promising for the hardware implementation of the reservoir computing. The performance can be further improved by introducing methods in the reservoir computing not included here, such as time multiplexing. In this paper, the effects of thermal fluctuations [33], which are large in nanometer-sized magnetizations, are not included. This issue is left for future work.



## ACKNOWLEDGMENTS

The authors would like to thank S. Tsunegi, M. Goto, K. Kudo, and R. Sato for valuable discussions.

### Appendix A: Synchronization of STOs in LLGS equation

We show an example of magnetization dynamics of STOs by solving the LLGS equation. The LLGS equation for the magnetizations of STO free layers  $\mathbf{m}_i$  ( $i = 1, 2, \dots, N$ ) normalized by the saturation magnetization  $M_s$  is given by

$$\frac{\partial \mathbf{m}_i}{\partial t} = -\gamma \mathbf{m}_i \times \mathbf{H}_i^{\text{eff}} + \alpha \mathbf{m}_i \times \frac{\partial \mathbf{m}_i}{\partial t} + \mathbf{T}_i^S, \quad (\text{A1})$$

where  $N$ ,  $t$ ,  $\gamma$ , and  $\alpha$  are the number of the STOs, time, gyromagnetic ratio, and Gilbert damping, respectively.  $\mathbf{H}_i^{\text{eff}}$  and  $\mathbf{T}_i^S = \sigma I_i \mathbf{m}_i \times (\mathbf{m}_i \times \mathbf{e}_p)$  are an effective field and spin-torque term with efficiency  $\sigma$ , current  $I_i$ , and unit vector in the direction of the spin polarization of the current  $\mathbf{e}_p$ , respectively.

In the example, we choose a typical STO with in-plane magnetized free and fixed layers having rectangular shape. Small ( $50^2 \times 10 \text{ nm}^3$ ) and thus uniform  $\mathbf{m}_i$  is assumed. A perpendicular field  $H_z$  is applied, yielding the out-of-plane precession (OPP) for large  $I_i$  [23]. The STOs are aligned on a square lattice, and all the magnetizations  $\mathbf{m}_i$  are coupled by the dipolar fields [40, 41].  $I_i$  and the initial directions of  $\mathbf{m}_i$  are randomized. Figure 7 shows an example of waveforms. Owing to the randomness, the waveforms are initially disordered. After several oscillation periods, the oscillations are synchronized. This state is obtained for other initial conditions, indicating the robustness of the synchronized state. Synchronization of vortex STOs coupled by the dipolar fields has been reported [27–29].

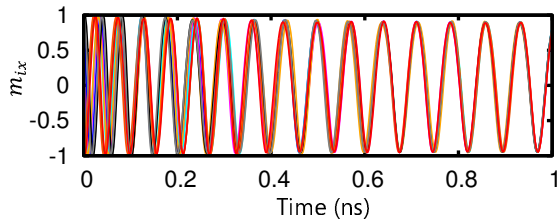


FIG. 7. Waveforms of  $m_{ix}$  of free layers of 9 STOs obtained by the LLGS equation.  $M_s = 1.6 \text{ kemu/cm}^3$ ,  $\alpha = 0.02$ , and  $H_z = 9 \text{ kOe}$ . Owing to  $H_z$ ,  $\mathbf{e}_p = (\cos 5^\circ, 0, \sin 5^\circ)$  is assumed. Neighboring STOs are separated by 50 nm. Mean and standard deviation of  $I_i$  are 20 mA and 0.2 mA, respectively. Initial directions of  $\mathbf{m}_i$  are randomized in the plane of  $m_{iz} = 0$ .

### Appendix B: From LLGS equation to nonlinear oscillator model

Here, we show the correspondence between the LLGS equation and the nonlinear oscillator model. In the OPP, the  $x$  and  $y$  components of  $\mathbf{m}_i$  are mainly oscillating and we introduce complex amplitudes  $\tilde{c}_i = m_{ix} - im_{iy}$ . From Eq. (A1), the equation of motion of  $\tilde{c}_i$  is

$$\frac{d\tilde{c}_i}{dt} = -i\gamma H_{iz}^{\text{eff}} \tilde{c}_i + i\gamma m_{iz} (H_{ix}^{\text{eff}} - iH_{iy}^{\text{eff}}) - \Gamma_i \tilde{c}_i, \quad (\text{B1})$$

where the term including  $\mathbf{H}_i^{\text{eff}}$  is exactly transformed while the damping and spin-torque terms are represented by using an effective damping rate  $\Gamma_i$ . Here, we assume uniform magnetizations in each STO. In the OPP,  $H_{iz}^{\text{eff}}$  mainly determines the precession axis and frequency  $\tilde{\omega}_i = \gamma H_{iz}^{\text{eff}}$ . Besides,  $H_{ix}^{\text{eff}} - iH_{iy}^{\text{eff}}$  is due to the dipolar fields from the other STOs. Although the prefactor includes  $m_{iz}$ , the prefactor depends little on  $\tilde{c}_i$ , because  $m_{iz}$  is almost constant for the OPP. The term including  $H_{ix}^{\text{eff}} - iH_{iy}^{\text{eff}}$  reduces to the coupling term as follows. We approximate for simplicity the free layer magnetization with volume  $V$  by a point magnetic moment  $\boldsymbol{\mu} = M_s V \mathbf{m}$ . The dipolar field at the place  $\mathbf{r} = (x, y, z)$  from this moment at the origin is given by

$$\mathbf{H} = \frac{\mu_0}{4\pi} \left[ 3 \frac{(\boldsymbol{\mu} \cdot \mathbf{r}) \mathbf{r}}{r^5} - \frac{\boldsymbol{\mu}}{r^3} \right], \quad (\text{B2})$$

with the permeability of vacuum  $\mu_0$ . Then,

$$H_x - iH_y = \frac{\mu_0 M_s V}{8\pi r^5} \times [(x^2 + y^2 - 2z^2) \tilde{c} + 3(x - iy)^2 \tilde{c}^* + 6(x - iy)zm_z]. \quad (\text{B3})$$

On the same plane  $\mathbf{r} = (x, y, 0)$ ,

$$H_x - iH_y = \frac{\mu_0 M_s V}{8\pi r^3} \left[ \tilde{c} + 3 \frac{(x - iy)^2}{r^2} \tilde{c}^* \right]. \quad (\text{B4})$$

Thus Eq. (B1) is written as

$$\frac{d\tilde{c}_i}{dt} = -i\tilde{\omega}_i \tilde{c}_i - i \sum_{j=1, j \neq i}^N (\Omega_{ij} \tilde{c}_j + \Xi_{ij} \tilde{c}_j^*) - \Gamma_i \tilde{c}_i, \quad (\text{B5})$$

with  $\Omega_{ij} = -\gamma m_{iz} \mu_0 M_s V / (8\pi |\mathbf{r}_i - \mathbf{r}_j|^3)$  and  $\Xi_{ij} = -3\gamma m_{iz} \mu_0 M_s V [x_i - x_j - i(y_i - y_j)]^2 / (8\pi |\mathbf{r}_i - \mathbf{r}_j|^5)$ . Here  $\mathbf{r}_i$  represents the place of the STO  $i$ .

We assume that the STOs generate with a common frequency  $\omega$  when isolated in steady state, and that the variation of the frequencies is caused by the nonlinear frequency shifts  $\delta\omega_i$ . Thus, the oscillation frequencies are represented by  $\tilde{\omega}_i = \omega + \delta\omega_i$ . Then, the uniform oscillation with the frequency  $\omega$  is decoupled by  $\tilde{c}_i = c_i e^{-i\omega t}$  as

$$\frac{dc_i}{dt} = -i\delta\omega_i c_i - i \sum_j (\Omega_{ij} c_j + \Xi_{ij} c_j^* e^{2i\omega t}) - \Gamma_i c_i. \quad (\text{B6})$$

Note that an oscillating factor with the frequency  $2\omega$  appears in the coefficient of  $c_j^*$ . This term does not affect

the dynamics of  $c_i$  when  $c_i$  varies slowly, as shown in the following. We assume that the time scale of the change of  $c_i$  is much longer than the oscillation period  $2\pi/\omega$  and  $c_i$  can be approximated by constant during  $2\pi/\omega$ . Then, by averaging Eq. (B6) for time  $\pi/\omega$ , the term including  $c_j^*$  vanishes owing to the factor  $e^{2i\omega t}$ , and hence the nonlinear oscillator model

$$\frac{dc_i}{dt} = -i\delta\omega_i c_i - \Gamma_i c_i - i \sum_{j=1, j \neq i}^N \Omega_{ij} c_j, \quad (\text{B7})$$

is obtained. This averaging is equivalent to using a variable

$$\bar{c}_i(t) = \frac{\omega}{\pi} \int_0^{\pi/\omega} dt' c_i(t + t'). \quad (\text{B8})$$

The numerical order of  $|\Omega_{ij}|$  is estimated as follows. In the typical case of  $m_{iz}^2 = 0.5$ ,  $M_s = 1.6 \text{ kemu/cm}^3$ , and  $V = 50^2 \times 10 \text{ nm}^3$ ,  $|\Omega_{ij}|$  is  $0.031 \text{ ns}^{-1}$  and  $0.25 \text{ ns}^{-1}$  for the center-to-center distance of 200 nm and 100 nm, respectively, indicating that  $|\Omega_{ij}|$  is of the order of  $0.01 \text{ ns}^{-1}$  to  $0.1 \text{ ns}^{-1}$ .

### Appendix C: NARMA task

Here, we show the performance in the NARMA task, where series defined by nonlinear recurrence relations are emulated, and ability to predict nonlinear time-series is

measured. We perform a NARMA task defined by the following equation:  $y_{k+1} = 0.4y_k + 0.4y_k y_{k-1} + 0.6s_k^3 + 0.1$  for  $s_k$  of uniform random numbers in  $(0, 0.2)$ , which is called NARMA2 task [7, 34]. We convert  $s_k$  to  $\xi_1(t)$  by a square wave with value  $\xi_1(t) = s_k - 0.1 \text{ ns}^{-1}$ . The performances are quantified by a normalized mean-squared error  $\epsilon = [\sum_k (\bar{y}_k - y_k)^2] / (\sum_k \bar{y}_k^2)$ , which is smaller when  $\bar{y}_k$  and  $y_k$  are closer, indicating higher performance.

The results of the NARMA2 task are shown in Fig. 8. The error for  $T_s = 20 \text{ ns}$  decrease with  $N$  by 3 orders, and the value of the error is comparable to previous studies [7].

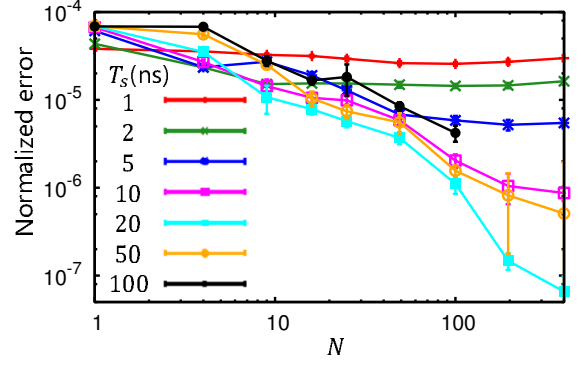


FIG. 8. Normalized mean-squared errors  $\epsilon$  in NARMA2 task as a function of  $N$  and  $T_s$ .

- 
- [1] H. Jaeger and H. Haas, Harnessing nonlinearity: Predicting chaotic systems and saving energy in wireless communication, *Science* **304**, 78 (2004).
  - [2] W. Maass, T. Natschlager, and H. Markram, Real-time computing without stable states: A new framework for neural computation based on perturbations, *Neural Comput.* **14**, 2531 (2002).
  - [3] D. Verstraeten, B. Schrauwen, M. D'Haene, and D. Stroobandt, An experimental unification of reservoir computing methods, *Neural Netw.* **20**, 391 (2007).
  - [4] L. Appeltant, M.C. Soriano, G. Van der Sande, J. Danckaert, S. Massar, J. Dambre, B. Schrauwen, C.R. Mirasso, and I. Fischer, Information processing using a single dynamical node as complex system, *Nat. Commun.* **2**, 468 (2011).
  - [5] L. Larger, M. C. Soriano, D. Brunner, L. Appeltant, J. M. Gutierrez, L. Pesquera, C. R. Mirasso, and I. Fischer, Photonic information processing beyond Turing: an optoelectronic implementation of reservoir computing, *Opt. Express* **20**, 3241 (2012).
  - [6] Y. Paquot, F. Duport, A. Smerieri, J. Dambre, B. Schrauwen, M. Haelterman, and S. Massar, Optoelectronic reservoir computing, *Sci. Rep.* **2**, 287 (2012).
  - [7] K. Fujii and K. Nakajima, Harnessing Disordered-Ensemble Quantum Dynamics for Machine Learning, *Phys. Rev. Appl.* **8**, 024030 (2017).
  - [8] D. Prychynenko, M. Sitte, K. Litzius, B. Krger, G. Bourianoff, M. Klui, J. Sinova, and K. Everschor-Sitte, Magnetic Skyrmion as a Nonlinear Resistive Element: A Potential Building Block for Reservoir Computing, *Phys. Rev. Appl.* **9**, 014034 (2018).
  - [9] R. Nakane, G. Tanaka, A. Hirose, Reservoir computing with spin waves excited in a garnet film, *IEEE Access*, **6**, 4462 (2018).
  - [10] T. Furuta, K. Fujii, K. Nakajima, S. Tsunegi, H. Kubota, Y. Suzuki, and S. Miwa, Macromagnetic Simulation for Reservoir Computing Utilizing Spin Dynamics in Magnetic Tunnel Junctions, *Phys. Rev. Appl.* **10**, 034063 (2018).
  - [11] S. I. Kiselev, J. C. Sankey, I. N. Krivorotov, N. C. Emley, R. J. Schoelkopf, R. A. Buhrman, and D. C. Ralph, Microwave oscillations of a nanomagnet driven by a spin-polarized current, *Nature* **425**, 380 (2003).
  - [12] A. N. Slavin and V. Tiberkevich, Nonlinear auto-oscillator theory of microwave generation by spin-polarized current, *IEEE Trans. Magn.* **45**, 1875 (2009).
  - [13] J. Torrejon, M. Riou, F. Abreu Araujo, S. Tsunegi, G. Khalsa, D. Querlioz, P. Bortolotti, V. Cros, K. Yakushiji, A. Fukushima, H. Kubota, S. Yuasa, M. D. Stiles, and J. Grollier, Neuromorphic computing with nanoscale spintronic oscillators, *Nature* **547**, 428 (2017).
  - [14] S. Tsunegi, T. Taniguchi, S. Miwa, K. Nakajima, K. Yakushiji, A. Fukushima, S. Yuasa, and H. Kubota, Evaluation of memory capacity of spin torque oscillator for re-

- current neural networks, *Jpn. J. Appl. Phys.* **57**, 120307 (2018).
- [15] D. Markovic, N. Leroux, M. Riou, F. Abreu Araujo, J. Torrejon, D. Querlioz, A. Fukushima, S. Yuasa, J. Trastoy, P. Bortolotti, and J. Grollier, Reservoir computing with the frequency, phase, and amplitude of spin-torque nano-oscillators, *Appl. Phys. Lett.* **114**, 012409 (2019).
- [16] F. Macia, A. D. Kent, and F. C. Hoppensteadt, Spin-wave interference patterns created by spin-torque nano-oscillators for memory and computation, *Nanotechnology* **22**, 095301 (2011).
- [17] T. Shibata, R. Zhang, S. P. Levitan, D. E. Nikonov, and G. I. Bourianoff, CMOS supporting circuitries for nano-oscillator-based associative memories, 13th Int. Workshop Cellular Nanoscale Netw. Appl. p. 1 (2012).
- [18] G. Csaba and W. Porod, Computational study of spin-torque oscillator interactions for non-boolean computing applications, *IEEE Trans. Magn.* **49**, 4447 (2013).
- [19] J. Grollier, D. Querlioz, and M. D. Stiles, Spintronic nanodevices for bioinspired computing, *Proceedings of the IEEE* **104**, 2024 (2016).
- [20] K. Kudo and T. Morie, Self-feedback electrically coupled spin-Hall oscillator array for pattern-matching operation, *Appl. Phys. Express* **10**, 043001 (2017).
- [21] D. Vodenicarevic, N. Locatelli, F. Abreu Araujo, J. Grollier, and D. Querlioz, A nanotechnology-ready computing scheme based on a weakly coupled oscillator network, *Sci. Rep.* **7**, 44772 (2017).
- [22] M. Romera, P. Talatchian, S. Tsunegi, F. Abreu Araujo, V. Cros, P. Bortolotti, J. Trastoy, K. Yakushiji, A. Fukushima, H. Kubota, S. Yuasa, M. Ernault, D. Vodenicarevic, T. Hirtzlin, N. Locatelli, D. Querlioz, and J. Grollier, Vowel recognition with four coupled spin-torque nano-oscillators, *Nature* **563**, 230 (2018).
- [23] S. I. Kiselev, J. C. Sankey, I. N. Krivorotov, N. C. Emley, M. Rinkoski, C. Perez, R. A. Buhrman, and D. C. Ralph, Current-Induced Nanomagnet Dynamics for Magnetic Fields Perpendicular to the Sample Plane, *Phys. Rev. Lett.* **93**, 036601 (2004).
- [24] T. Kanao, H. Suto, K. Kudo, T. Nagasawa, K. Mizushima, and R. Sato, Transient magnetization dynamics of spin-torque oscillator and magnetic dot coupled by magnetic dipolar interaction: Reading of magnetization direction using magnetic resonance, *J. Appl. Phys.* **123**, 043903 (2018).
- [25] Z. Zeng, G. Finocchio, B. Zhang, P. Khalili Amiri, J. A. Katine, I. N. Krivorotov, Y. Huai, J. Langer, B. Azzerboni, K. L. Wang, and H. Jiang, Ultralow-current-density and bias-field-free spin-transfer nano-oscillator, *Sci. Rep.* **3**, 1426 (2013).
- [26] H. Kubota, K. Yakushiji, A. Fukushima, S. Tamaru, M. Konoto, T. Nozaki, S. Ishibashi, T. Saruya, S. Yuasa, T. Taniguchi, H. Arai, and H. Imamura, Spin-torque oscillator based on magnetic tunnel junction with a perpendicularly magnetized free layer and in-plane magnetized polarizer, *Appl. Phys. Express* **6**, 103003 (2013).
- [27] A. D. Belanovsky, N. Locatelli, P. N. Skirdkov, F. Abreu Araujo, J. Grollier, K. A. Zvezdin, V. Cros, and A. K. Zvezdin, Phase locking dynamics of dipolarly coupled vortex-based spin transfer oscillators, *Phys. Rev. B* **85**, 100409(R) (2012).
- [28] N. Locatelli, A. Hamadeh, F. Abreu Araujo, A. D. Belanovsky, P. N. Skirdkov, R. Lebrun, V. V. Naletov, K. A. Zvezdin, M. Muoz, J. Grollier, O. Klein, V. Cros, and G. Loubens, Efficient synchronization of dipolarly coupled vortex-based spin transfer nano-oscillators, *Sci. Rep.* **5**, 17039 (2015).
- [29] V. Flovik, F. Maci, and E. Wahlström, Describing synchronization and topological excitations in arrays of magnetic spin torque oscillators through the Kuramoto model, *Sci. Rep.* **6**, 32528 (2016).
- [30] J. C. Slonczewski, Current-driven excitation of magnetic multilayers, *J. Magn. Magn. Mater.* **159**, L1 (1996).
- [31] T. Kanao, T. Nagasawa, K. Kudo, H. Suto, M. Yamagishi, K. Mizushima, and R. Sato, Effects of power fluctuation on fast magnetic field detection using a spin-torque oscillator, *Appl. Phys. Express* **9**, 113001 (2016).
- [32] A. N. Slavin and V. S. Tiberkevich, Theory of mutual phase locking of spin-torque nanosized oscillators, *Phys. Rev. B* **74**, 104401 (2006).
- [33] M. Quinsat, D. Gusakova, J. F. Sierra, J. P. Michel, D. Houssameddine, B. Delaet, M.-C. Cyrille, U. Ebels, B. Dieny, L. D. Buda-Prejbeanu, J. A. Katine, D. Mauri, A. Zeltser, M. Prigent, J.-C. Nallatamby, and R. Sommet, Amplitude and phase noise of magnetic tunnel junction oscillators, *Appl. Phys. Lett.* **97**, 182507 (2010).
- [34] A. F. Atiya and A. G. Parlos, New results on recurrent network training: Unifying the algorithms and accelerating convergence, *IEEE Trans. Neural Networks* **11**, 697 (2000).
- [35] J. Dambre, D. Verstraeten, B. Schrauwen, and S. Massar, Information processing capacity of dynamical systems, *Sci. Rep.* **2**, 514 (2012).
- [36] Y. Kuramoto and I. Nishikawa, Statistical macrodynamics of large dynamical systems. Case of a phase transition in oscillator communities, *J. Stat. Phys.* **49**, 569 (1987).
- [37] J. A. Acebrn, L. L. Bonilla, C. J. Prez Vicente, F. Ritort, and R. Spigler, The Kuramoto model: A simple paradigm for synchronization phenomena, *Rev. Mod. Phys.* **77**, 137 (2005).
- [38] T. E. Lee, H. Tam, G. Refael, J. L. Rogers, and M. C. Cross, Vortices and the entrainment transition in the two-dimensional Kuramoto model, *Phys. Rev. E* **82**, 036202 (2010).
- [39] P. C. Matthews and S. H. Strogatz, Phase Diagram for the Collective Behavior of Limit-Cycle Oscillators, *Phys. Rev. Lett.* **65**, 1701 (1990).
- [40] K. Kudo, T. Nagasawa, H. Suto, T. Yang, K. Mizushima, and R. Sato, Influence of dynamical dipolar coupling on spin-torque-induced excitations in a magnetic tunnel junction nanopillar, *J. Appl. Phys.* **111**, 07C906 (2012).
- [41] K. Kudo, H. Suto, T. Nagasawa, K. Mizushima, and R. Sato, Resonant magnetization switching induced by spin-torque-driven oscillations and its use in three-dimensional magnetic storage applications, *Appl. Phys. Express* **8**, 103001 (2015).